ACES Asian Chemical Editorial Society

doi.org/10.1002/cnma.202200451

CHEMNANOMAT
Research Article

www.chemnanomat.org

Tuning the Electromagnetic Shielding Mechanism with Nitrogen-doped Graphene Aerogels

Marcos Álvarez, Juan Baselga, and Javier Pozuelo*[a]

Abstract: The electromagnetic shielding efficiency of a given material can be quantified as the sum of three contributions: reflection, absorption, and multiple reflections, which under certain conditions can be reduced to the first two, which are the main shielding processes decisive for its further application. A simple process to prepare nitrogen-doped graphene aerogels followed by subsequent thermal treatments is proposed to adapt and control the shielding mechanisms that take place to the possible requirements of the system. Nitrogen-doped aerogels are prepared by the addition of urea in the hydrothermal synthesis and subsequent heat treatments at 500 and 1000 °C. Reflection/absorption power ratio values of unity down to values as low as 0.2 are obtained. This study represents an advance in electromagnetic shielding materials and the adaptation of these to the needs of different applications, reducing the traditional negative environmental impact of these devices.

Introduction

Electromagnetic interferences (EMI) are waves normally produced by electronic devices that may mean a deterioration of the performance of other electronic components, making them one of the main working obstacles to deal with in daily life and industrial activity.[1]

When an electromagnetic wave impacts a material, two different signals are generated: a reflected wave related to the impedance mismatch between receptor and source environments, and a transmitted wave headed to the interior of the material. The transmitted wave partially dissipates as heat, because of the Joule effect, and partially reflects each time encounters a surface in its way; the set of reflection processes from all the planes inside the material is called multiple reflections. These reflected and transmitted waves inside the material may cause constructive or destructive interferences depending on the sample thickness and wave frequency.[2] Consequently, the electromagnetic shielding efficiency of a certain material can be quantified as the sum of three contributions: reflection, absorption, and multiple reflections. Taking advantage of one or more of them, material performance can be optimized for specific EMI shielding applications although, most of the time absorption is desired as the main shielding mechanism because of the possible interference problems caused when the incident wave is reflected by the receptor shielding material.[3] Consequently, the use of EMI absorbing materials is one of the most practical ways of shielding radiation. The design of a 3D material (instead of a thin 2D film) with reduced impedance mismatch (with, for example, high porosity) and with high electrical conductivity (being advanced carbon materials potential candidates as raw materials) would be optimal for this purpose.[4]

During the last years, numerous research efforts on EMI shielding materials have focused on the production of highly conductive carbon aerogels, mainly developed by self-assembly techniques of carbon-based nanomaterials.[5] Outstanding results were obtained in previous works[6,7] (total shielding efficiency SE_T more than 20 dB all along the frequency range between 1 and 18 GHz) when using CVD-growth carbon nanotube (CNT) foams prepared by one- or two-stage freezing and lyophilization with similar objectives, while other publications have explored the use of graphene and lately the new titanium carbide structures called MXenes.[8,9] Among the works related with this last topic, is especially relevant the extensive collection of works carried out by Gogotsi et al. or the interesting works of Liang et col. where highly conductive-high attenuation composites were prepared combining MXenes with CNTs, to obtain SE_T values of more than 90 dB.[10,11] Among all these approaches, graphene is probably the one that offers a wider set of possibilities and, consequently, has attracted more attention. 3D porous structures of graphene materials may trap or attenuate EM radiation through the multiple and complex conductive paths in its structure. As an example of graphene's great potential, Zhang et col. reached absorption shielding efficiency SE_A values up to 34 dB making use of graphene foams produced by a self-assembly method.[12]

Despite the high shielding performance observed when using graphene as the main component of aerogel monoliths, multiple studies have explored the use of different electronic dopants to improve their performance and modulate pore size and shape. Nitrogen-doped graphene aerogels have been widely employed showing some promising results.[13–16] N doping can decrease the electrical resistance of graphene

[a] M. Álvarez, Prof. J. Baselga, Prof. J. Pozuelo
Departamento de Ciencia e Ingeniería de Materiales e Ingeniería Química (IAAB), Universidad Carlos III de Madrid, Leganés, Madrid, 28911 (Spain)
3 m.es
E-mail: jpozue@ing.uc

Supporting information for this article is available on the WWW under https://doi.org/10.1002/cnma.202200451

easing electron transfer processes. Nitrogen atoms may break the sp^2 configuration of graphene generating sp^3 defects giving raise to defect polarization and electronic dipole polarization relaxation, improving dielectric loss and, consequently, increasing the EMI absorption mechanism.[14] There are four possible N doping paths: pyrrolic, pyridinic, graphitic, and oxidized pyridinic bonding. Li et col. explained that pyrrolic N bonding can dramatically increase the electron concentration in graphene by introducing five-membered heterocyclic rings and sp^3 hybridization and Zhou et col. found an increased EMI absorption in the Ku band (12-18 GHz) of graphene-wax aerogels doped by a simple hydrothermal treatment using ethylenediamine (EDA) as a nitrogen source.[14,17] Many papers have explored the use of NH_3 gas as a nitrogen source through a CVD process as reported by Qing et col. or Zan et col.; in these cases, the main limitation was the control of the amount of N introduced in the structure.[18,19] Urea has also been used as an N source due really high content of N, which also offers the possibility of tunning through reaction temperature selection in a very accurate way the number and presence of different species, a condition that has a direct impact on the electrical conductivity.[20,21] Urea also allows to ensure internal doping of the graphene lattice, against other options where a gaseous N source is used, and the doping is produced more on the surface of the graphene structure.[22] The simpleness of its use, and the ability to tune the amount and configuration of the N doping atoms, which could be easily scalable, linked to the relatively low price and abundance of this substance, make urea a perfect candidate as an extensively used N dopant source in the industry.[23]

The use of urea as the N source consists of the liberation of isocyanic acid and NH_3 below 190 °C. Isocyanic acid reacts with hydroxyl groups from the graphene oxide (GO) used as starting raw material, to form at a middle step, after the dehydration and reordering processes, pyrrolic nitrogen.[13] Other reaction intermediates and products such as cyanuric acid, melamine, or ammelide may be or not be involved in the doping processes depending on the reaction temperature.[24]

The correct stacking of graphene sheets is also a critical factor to increase the absorption shielding efficiency (SE_A) since forming a large conductive interconnected network of graphene sheets will improve the total shielding efficiency.[25] In this context, when urea is added to the graphene dispersion more ordered structures are obtained and graphene layers seem to be thinner and more separated.[26] Moon et coll. have demonstrated the efficiency of the hydrothermal synthesis method and an extra thermal treatment on the porosity and the electrical conductivity of graphene aerogels.[16] All along this process the number of oxygenated functional groups decreases causing a high hydrophobic interaction between the reduced graphene oxide (rGO) layers; these interactions induce graphene/water phase separation driving one eventual gelation of the system. The reduction process taking place during the hydrothermal treatment consists of the deprotonation of GO at relatively low temperatures inside an autoclave.[2] Urea molecules begin to decompose at 150 °C and, after the synthesis, during additional heat treatment, excess urea mainly decomposes into gaseous NH_3 and CO_2 that help to separate graphene layers, preventing their restacking and increasing the conductivity.[20]

In this work, graphene has been selected as a building material to prepare highly conductive porous aerogels and following the works of Liu et col. the addition of urea as an agent for EMI shielding optimization has been explored.[27,28] For these purposes, a new path to producing N-doped reduced graphene oxide (rGO) aerogels is proposed. Starting with graphite powder we obtain GO, which is used to prepare urea containing rGO hydrogel monoliths. The main difference with previous works is the introduction of a pre-freezing step before the hydrothermal treatment, as a way of facilitating gelation and improving the organization of the hydrogel porosity, and the use of higher annealing temperatures in a reductive atmosphere after the synthesis to study its effect on the mechanism of N-doping. The effect of the different processing parameters (quantity of dopant and thermal treatment temperature) on graphene aerogels structure is explored, and a relation between them and a wide range of shielding efficiency parameters (SE, % transmitted, reflected, and absorbed power) is searched.

Results and discussion

Figure 1 shows optical and SEM images of the cross sections of some of the aerogels. These images were taken in a cross-section orthogonal to the cylinder axis of the aerogels obtained by hydrothermal synthesis. In every case, the pore shape changes from a more flattened morphology parallel to the external perimeter of the cylinder to a more equiaxial form at the aerogel centre, where the longitudinal axis of the sponge crosses the plane. This fact could be explained as an effect of compression forces affecting the sample during the hydrothermal synthesis process. These stresses, decrease the cylinder radius, making it more compact and reducing the sphericity of the pores present in the most outlying areas. The pore size of all aerogels was analysed (Table S1) with the help of ImageJ software.[29] No major changes in pore size were observed and these variations are more a result of the irregularity of the pores than an effect of the doping process.

The X-ray diffractograms of graphite, GO, GR_N0 and GR_N2 are shown in Figure S2. It is possible to observe how after the oxidation process the characteristic signals of graphite disappear and how the diffraction of the (002) plane, which in graphite appears at $2\theta = 26°$, shifts to $2\theta = 11°$ in GO. This change corresponds to an increase in the interplanar distance from 0.34 nm to 0.80 nm due to the inclusion of oxygenated functional groups, mainly alcohols, epoxy, and acid. The dispersion process causes the separation of the graphene sheets and the hydrothermal synthesis causes a gelation and reduction process of the graphene oxide which results in a flat signal (002). The graphene sheets are separated by a bigger distance than graphite, resulting in a lower 2θ value. It can also be observed in Figure S2a slight increase in the (002) diffraction for doped samples: 2θ varies from 24.0° for GR_N0 to 25.6°,

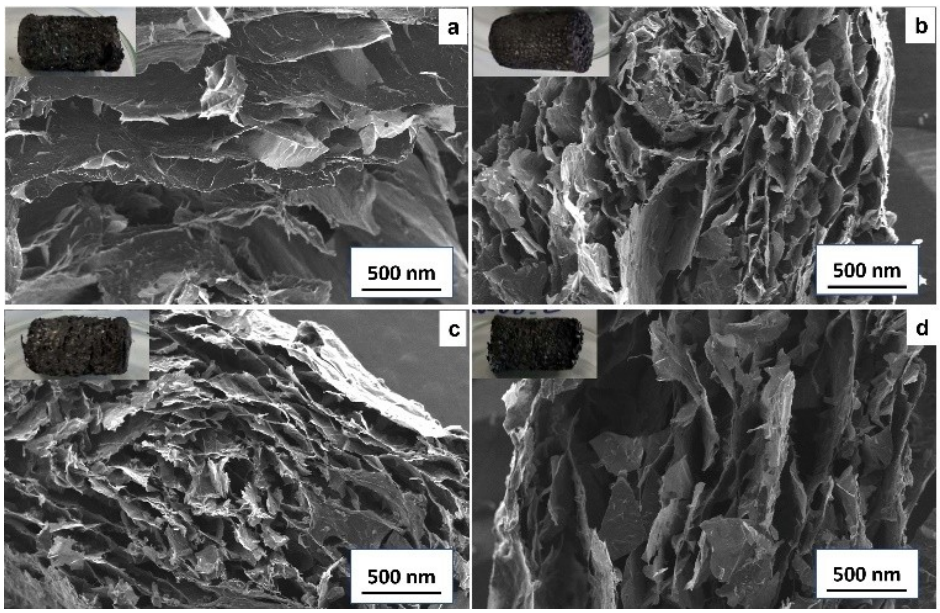

Figure 1. Optical and SEM images of GR_N0 (a), GR_N2 (b), GR_N2:500 (c) and GR_N2:1000 (d).

26.2°, 26.1° for GR_N1, GR_N2, GR_N3 samples respectively, mainly due to the nitrogen doping of the graphene sheets as primary and secondary amines.

Elemental analysis of the aerogels formed by hydrothermal synthesis with different amounts of urea is shown in Table 1. To study how nitrogen content is modified by thermal treatments, sample GR_N2 was selected, and the results are also presented in Table 1. It is possible to observe that the amount of nitrogen increases with the initial content of nitrogen dopant; however, although the amount of urea is tripled, nitrogen content in the aerogel increases only from 5.6 to 6.3% suggesting a possible saturation of the anchoring sites of nitrogen atoms on the graphene surface. It can also be observed that the proportion of oxygen atoms decreases as nitrogen content increases, possibly due to substitution reactions of hydroxy and epoxy groups, which are removed in hydrothermal synthesis leaving active positions for nitrogen doping, especially primary and secondary amines.[30,31]

As expected, the amount of nitrogen and oxygen atoms decreases with increasing temperature of the heat treatment as reflected by the composition variation of samples GR_N2, GR_N2:500 and GR_N2:1000. However, oxygen content strongly drops from 17.5% to 6.2% while nitrogen content decreases only from 6.0% to 3.4%. This effect could be due to the higher thermal stability of the nitrogen atoms in the carbon lattice of graphene by the formation of tertiary amines when substituting atomic carbon positions with graphitic, pyridinic and pyrrolic nitrogen.

Figure 2 shows the different types of nitrogen bonding that can be found in nitrogen-doped graphene. Graphitic nitrogen refers to substitutional N. Pyridinic nitrogen refers to the bond between N and two C atoms at the defects or edge of the graphene lattice. As pyridinic, pyrrolic nitrogen is another form of aromatic N insertion that increases the electron density of graphene. Pyridinic N-oxides can often be observed in N-doped graphene synthesized from GO due to a large amount of alcohol and epoxy groups in GO.[28,32,33]

XPS has been used to study doping and bonding in samples GR_N2, GR_N2:500 and GR_N2:1000. Figure 3 shows the XPS

Table 1. Relative weight quantification in % measured by elemental microanalysis of C, H, N and O for all the samples after hydrothermal synthesis and GR_N2 samples after thermal treatment.

Sample	C [%]	H [%]	N [%]	O [%]
GR_N0	73.0	2.7	0.0	24.3
GR_N1	74.7	1.8	5.6	17.9
GR_N2	74.9	1.6	6.0	17.5
GR_N2:500	84.5	1.3	5.4	8.8
GR_N2:1000	89.42	1.0	3.4	6.2
GR_N3	74.1	1.6	6.3	18.0

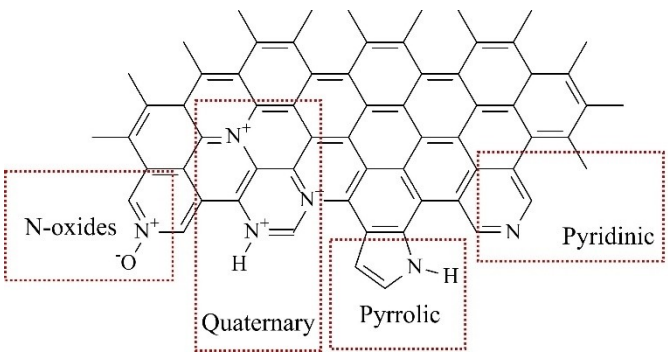

Figure 2. Scheme of N doping configurations in graphene structure.

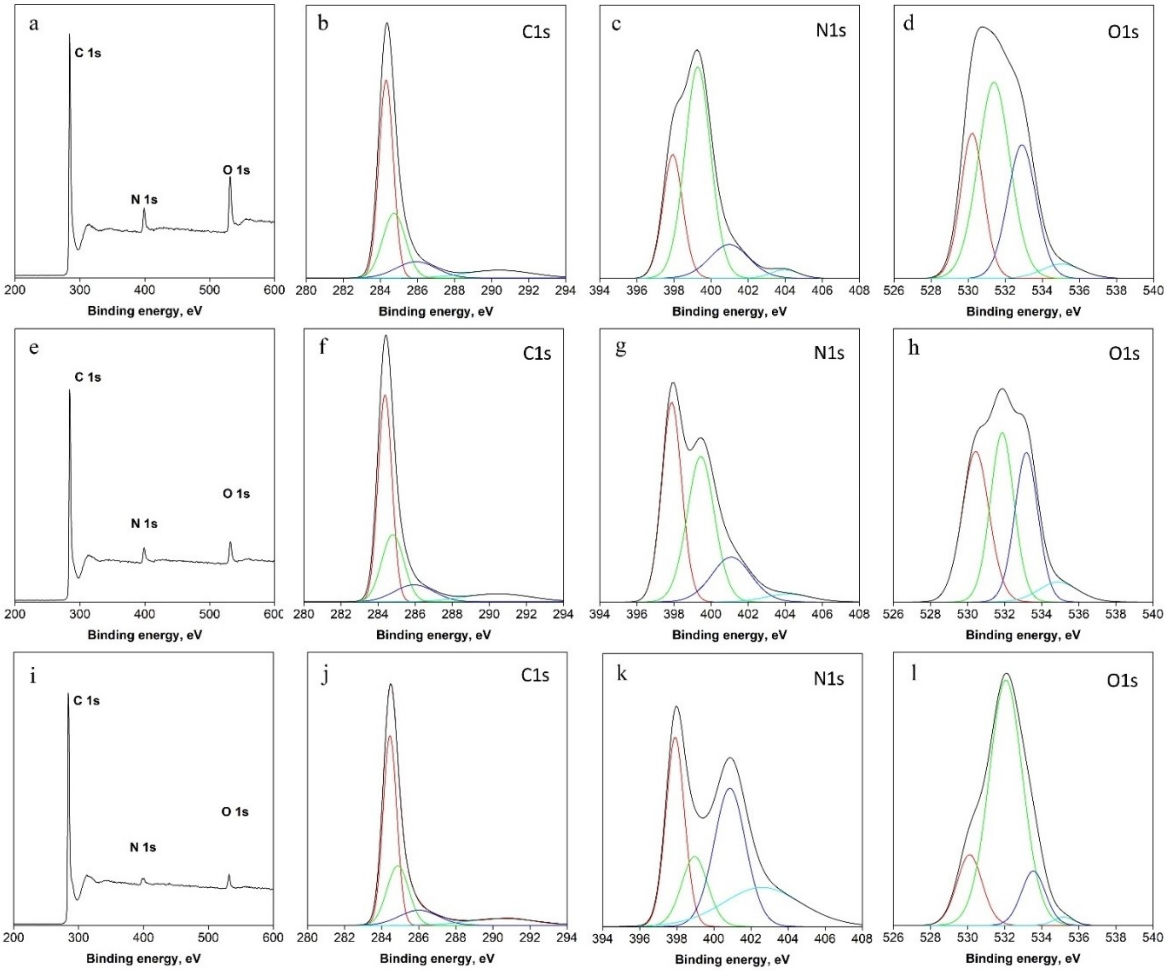

Figure 3. XPS spectra of GR_N2 (a,b,c,d); GR_N2:500 (e,f,g,h); GR_N2:1000 (i,j,k,l); deconvolution of C1s (b,f,j); deconvolution of N1s (c,g,k) and deconvolution of O1s (d,h,l)

spectra of these three samples in which the three peaks that correspond to the energy of the C 1s, N 1s and O 1s electronic orbitals can be identified at 284, 400 and 534 eV respectively.

The spectrum corresponding to C 1s can be fitted to four Gaussian signals, centred at 284.40, 285.39, 286.41 and 289.90 eV. The first signal, centred at 284.40 eV, corresponds to graphite-type sp^2-hybridised C atoms. The second signal, centred at 286.41 eV, can be assigned to sp^3-hybridised C atoms bonded to nitrogen or oxygen.[16] The third signal, centred at 285.39 eV, can be assigned to sp^2-hybridised carbon atoms bonded to nitrogen or oxygen. A fourth signal appears that unlike N-doped graphene grown directly by the CVD system,[14,17,34] the fourth signal at 289.90 eV is observed in our sample, possibly due to pyridinic nitrogen oxides.[35,36] In research on nitrogen-doped graphene, the N1s spectrum usually deconvolutes into three individual peaks that are assigned to pyridinic nitrogen (398.1–399.3 eV), pyrrolic nitrogen (399.8–401.2 eV), and quaternary nitrogen (401.1–402.7 eV) with the position varying over a relatively wide range in different studies.[31,34,36] The charge of the nitrogen and its neighbouring atoms and the redistribution of electrons after ionization will influence the precise position of the different types of nitrogen. In addition to these three types of nitrogen, in systems with graphene oxide, the peak corresponding to the N-oxides of pyridinic N is also observed at ~402.8 eV in several studies. The O1s signal can be deconvoluted to four signals. The first signal at 530.5 eV is due mainly to double bonds with ketone-type carbon atoms. A second signal at 532.0 eV which we attribute to the formation of oxides with nitrogen. The third signal at 533.3 eV is mainly due to single bonds with carbon atoms, such as anhydrides, esters, ethers, and alcohols/phenols. The fourth signal at 535.3 eV is due mainly to carboxylic groups.

Table 2 shows the amount of each of the specific bonding configurations of C, N and O atoms for sample GR_N2 both as prepared and thermally treated at 500 and 1000 °C. As expected, thanks to elemental analysis (Table 1), the overall content of heteroatoms decreases with the heat treatments although the specific bonding change significatively with temperature.

Although all types of bonding are present, Table 2 clearly shows that N atoms in the as-prepared sample, which has been subjected to and hydrothermal process at 180 °C, are mainly of

Table 2. XPS atomic quantification of different bonding configurations of C, N and O inside the atomic structure of GR_N2, GR_N2:500 and GR_N2:1000 samples.

	GR_N2 [%]	GR_N2:500 [%]	GR_N2:1000 [%]
C	86.3	90.9	95.2
C=C	53.3	52.8	53.9
C–O, C-N	28.8	28.1	28.1
C=O, C=N	14.2	13.7	14.2
C–N(oxides)	11.8	11.4	11.8
N	8.1	4.6	2.4
N(pyridine)	25.7	39.3	27.6
N(pyrrolic)	57.7	39.5	14.3
N(quaternary)	14.1	17.6	34.3
N(oxides)	2.5	3.6	23.8
O	5.6	4.3	2.2
O(C=O)	23.8	33.0	15.5
O(N(oxides))	45.1	32.5	71.7
O(C–O)	28.1	28.1	11.3
O(COO)	4.0	6.4	1.5

the pyrrolic type, and O atoms are mainly bonded to N atoms forming oxides. The former is electron donating groups while the latter electron-withdrawing and the overall effect on DC conductivity will probably be partially balanced. When the sample is treated at 500 °C pyrrolic N atoms seem to transform into the more stable pyridinic form and both forms account for almost 80% of all N atoms. On heating at 1000 °C, pyrrolic forms become a minority in the remaining N atoms. It is notable fact that the majority of remaining O atoms are in the form of electron-withdrawing N-oxides.

Figure 4 shows the DC electrical conductivity values obtained for all samples. We can see how in the samples without heat treatment the introduction of urea in the hydrothermal synthesis decreases the conductivity. Possibly this effect is due to the introduction of non-integrated groups into the hexagonal structure of graphene. The heat treatment at 500 °C causes an increase in the electrical conductivity in all samples, however, it does not reach the values of the graphene oxide sample. Possibly, the 500 °C treatment eliminates pyridinic and pyrrole groups but does not produce the electronic reorganization necessary to produce an increase in conductivity. The heat treatment at 1000 °C does cause a considerable increase in conductivity, this effect may be due to the increase in quaternary nitrogen and nitrogen that form oxides as can be seen in the tendency observed in Figure S4a). These atoms are positive doping in the reduced graphene oxide structure and an increase in the ratio Q:P expressed in equation 1S leads to a considerable increase in electrical conductivity.

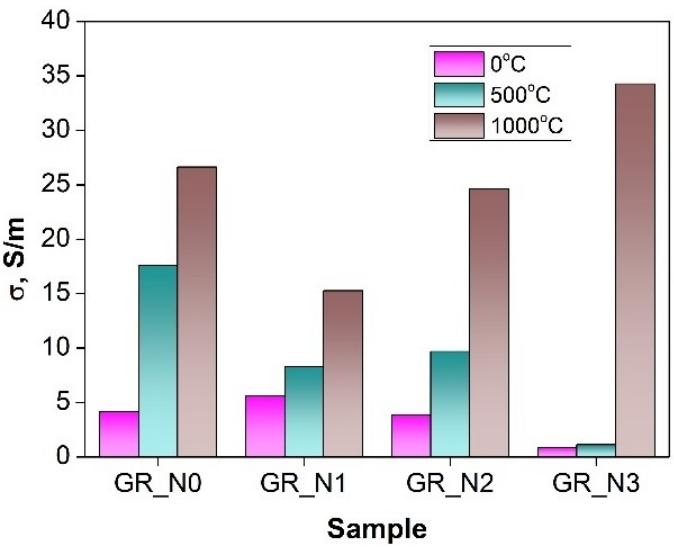

Figure 4. DC electrical conductivity of all the samples with and without post-heat treatment.

The development of an electromagnetic shielding material requires an initial evaluation of the reflection and absorption coefficients. As explained in point 4.3, these coefficients determine the relationship between the reflected, absorbed, or transmitted power concerning the power of the incident radiation. These coefficients are highly dependent on the conductivity of the sample. For materials with high conductivity, both the reflection and absorption processes will be significant, but, if the reflection coefficient is high, the fraction of the incident wave that can enter the material will be small and therefore the absorption coefficient will decrease.[4] A closely related factor in explaining electromagnetic behaviour is porosity. Tunning porosity in conductive systems makes it possible to adapt the impedance mismatch between the medium and the material. If the porosity is increased the material becomes less reflective, and a greater proportion of the electromagnetic wave can enter the material to be absorbed.

Figure 5 shows the ratio between the mean values of reflection and absorption coefficients for the studied samples. It is possible to observe how there is an increase in this relationship when increasing the heat treatment temperature. The increase in the heat treatment causes a graphitization of the pore walls which leads to an increase in the conductivity. The increase in conductivity increases the impedance difference between the medium and the sample, which leads to an increase in reflection. As mentioned above, an increase in reflection means that a smaller proportion of the electro-

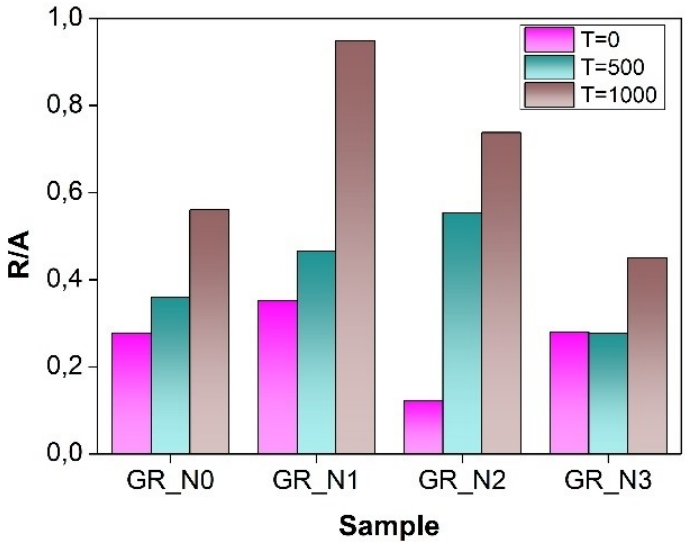

Figure 5. Reflection/absorption ratio for all samples.

magnetic radiation can enter the material and therefore absorption decreases.

Figure 6 shows these coefficients for all the samples as a function of frequency. In all of them, the reflection coefficient is always lower than the absorption coefficient, so it can be said that the most important mechanism is the absorption of electromagnetic radiation for all the studied samples. Figure 6 shows how N inclusion improves the absorptive behaviour of GR samples, increasing absorbed power, but also producing a slight increase of transmitted power. This unwanted effect can be corrected by applying thermal treatment, as seen in the results for samples GR_N2:1000. Figure S5 shows that in general, N doping improves absorptive behaviour in all the studied amounts of dopant.

A striking behaviour of the nitrogen-doped, and heat-treated samples at 1000 °C (GR_N1:1000, GR_N2:1000, GR_N3:1000) can be seen in Figure S5. The results of image treatment calculations to determine the pore size shown in Table S1 show that there are no considerable changes in pore size in any of these three samples. The bulk densities of these three samples joined together in Table S2 do not show any remarkable change either. The conductivity of these samples increases, as shown in Figure 4, as the nitrogen content increases, so we would expect an increase in the R/A ratio, but we find just the opposite. We can therefore affirm that the introduction of nitrogen atoms into the graphene structure generates absorption points that decrease the R/A ratio and make the materials less reflective and more absorbent of radiation. With these results, we could find a new method to alter the processes of reflection and absorption of electromagnetic radiation. The reflection-absorption of electromagnetic radiation will depend on the conductivity of the sample, the size of the pores and the presence of atomic impurities embedded within the hexagon lattice of graphene.

Figure 7 shows the electromagnetic efficiency values (a concept that is defined in point 4.3) for samples with and without N doping and with thermal treatments. Absorption electromagnetic efficiency SE_A is considerably higher than the reflected contribution SE_R for all samples. According to equation 4, SE_A is determined by the portion of the electromagnetic wave that penetrates inside the material; therefore, it can be stated that the preferential mechanism of deactivation is the absorption of the radiation in all of them. However, the existence of a reflection process means that only a portion of the radiation penetrates the material to be absorbed and is therefore decisive in obtaining radiation-absorbing materials. SE_A values of samples with a high reflection effect should not be reliable. If the R/A ratio is taken as an indicator of the importance of the reflection mechanism, it can be said that samples containing urea as obtained after hydrothermal synthesis have the lowest reflective contributions and, therefore, the bigger contribution to absorption EMI shielding. Among all the cases where the R/A ratio is low, samples GR_N2 and GR_N3 are especially remarkable because the ratio is lower than 0.3 in both cases. On the other hand, despite having high power absorption values, reflection is too low in these cases and therefore total shielding effectiveness SE_T is too low, being these values all along the studied frequency range around 10 dB. Looking at SE values in Figure 7, a significant increment in the overall SE_T can be obtained if annealing is performed after the synthesis, especially at 1000 °C, where the reflection contribution grows moderately rising SE_T above 20 dB during all the frequency range and reaching about 30 dB close to 18 GHz with a R/A ratio lower than 0.8 in the two cases. In the case of GR_N1, even higher SE_T values up to 35 dB near 18 GHz can be reached if annealing is performed at 1000 °C, but the R/A ratio reaches almost 1, making the material to be almost more reflective than absorbing.

This phenomenon, where samples with urea and thermal treatment at 1000 °C have the best and most reliable SE_T, could be explained by an appropriate balance between porosity and conductivity: compositional change due to the reduction of functional groups and better graphitization of the sp^2 network.

Figure S6 shows how both real and imaginary contributions of permittivity decrease when adding N to the rGO structure and how both increase when applying successive thermal treatments to the aerogels. These results are consistent due to the known relationship between both parameters with the dipolar moment and electrical conductivity of the samples, which are directly proportional to the reduction degree of rGO structure.[37] Dipolar polarization decreases when increasing N content if no thermal treatment is applied, this is due to the fact of N dopant atoms at low temperatures mainly act as pyrrolic N disturbing the induced overall electric dipole moment of the material, decreasing conductivity and easing EMI absorption.[38] When thermal treatments are applied, N bonding configuration changes to graphitic and pyridinic nitrogen easing the necessary dipole moment changes to increase the overall dipole polarization and conductivity, increasing real and imaginary permittivity.

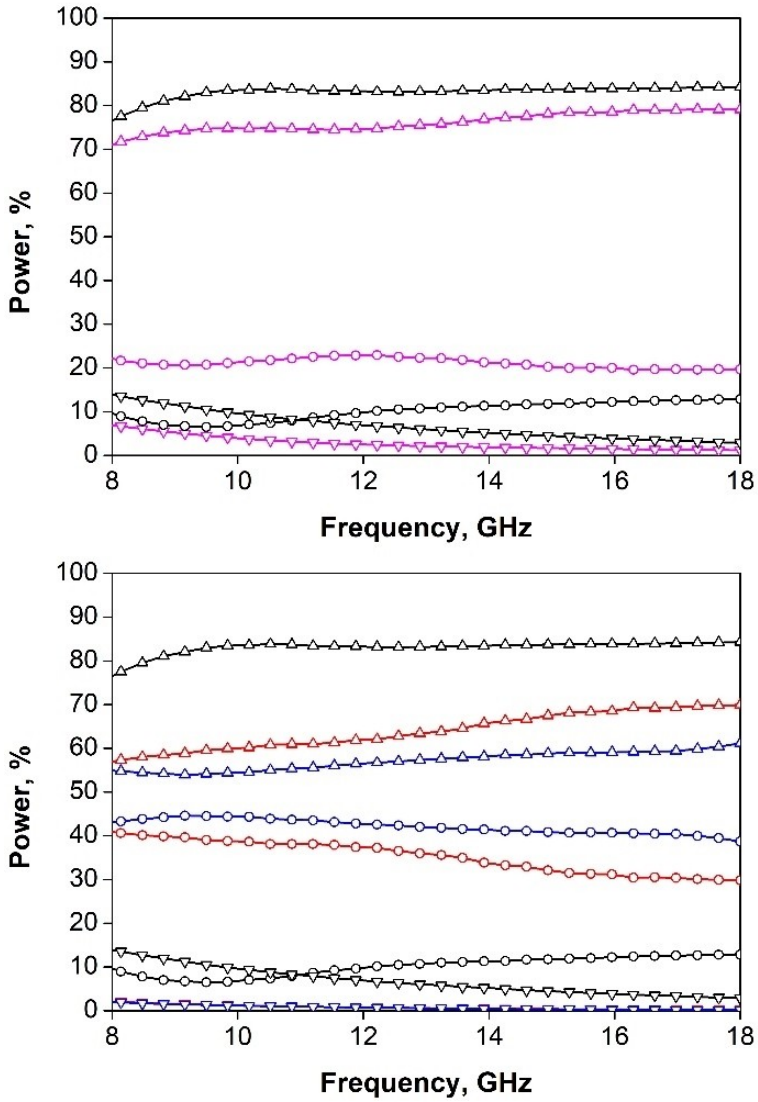

Figure 6. Power coefficients: reflection (–O–), absorption (–Δ–), transmission (-∇-). GR_N0 (cyan), GR_N2 (black), GR_N2:500 (red), GR_N2:1000 (blue).

Conclusion

A method to manufacture highly porous and highly absorbing N-doped rGO aerogels has been developed through the following sequence of processes: dispersion, freezing, hydrothermal synthesis, and lyophilization. The preparation of hydrogels by hydrothermal synthesis in the presence of urea results in porous structures with apparent densities in the order of 20 mg/cm^3. The amount of nitrogen introduced, and subsequent heat treatment allows the conductivity of the aerogel and consequently the electromagnetic shielding mechanism to be modified. The reflection-absorption ratio of electromagnetic radiation depends on the conductivity of the sample, the size of the pores and the presence of atomic impurities embedded within the hexagon lattice of graphene. Pyrrolic nitrogen inclusion (obtained at low temperatures) improves absorption by the reduction of the overall electric dipole moment of rGO, but its coexistence with quaternary and pyridinic N (obtained at higher temperatures) can improve reflection with a slight decrease of EMI absorption to get SE_T values up to almost 35 dB in thermally treated rGO doped samples.

Experimental section

Materials and methods

Graphite powder (with a purity $>$99.999%) was acquired from Alfa Aesar and urea (with a purity $>$99%) from Sigma-Aldrich. The hydrogenated derivative of diglycidyl ether of bisphenol-A (HDGE-BA) epoxy resin was purchased to CVC Specialty Chemicals (USA); its epoxy equivalent mass was 210 g·mol^{-1} determined by acid titration. m-Xylylene diamine (Sigma-Aldrich) was used as a curing agent. H_2O_2 30% w/v (Panreac), $KMnO_4$ (Panreac), $NaNO_3$ (Sigma-Aldrich), and H_2SO_4 98% v/v (Panreac) were employed for graphite oxidation and used without any further purification.

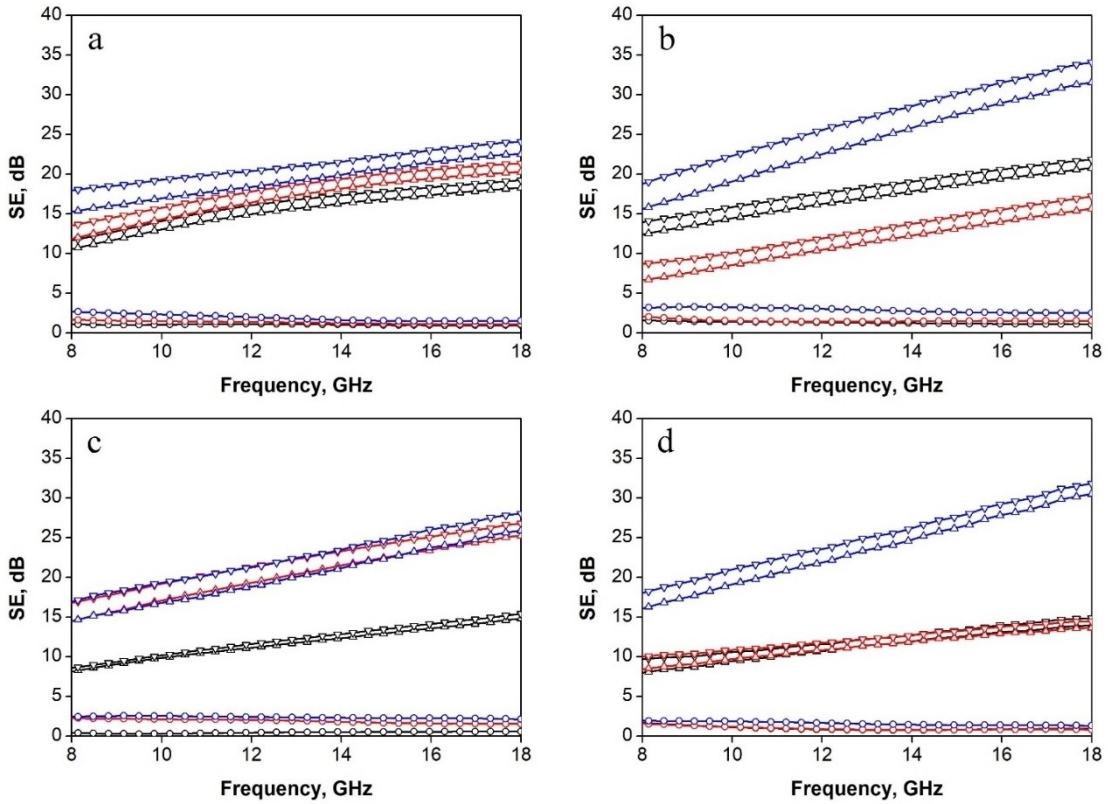

Figure 7. Electromagnetic efficiency for GR–N0 (a), GR–N1 (b), GR–N2 (c), GR-N3 (d); SE_R (–O–), SE_A (–Δ–), SE_T (-∇-) without (black), and with thermal treatment T = 500 °C (red), T = 1000 °C (blue)

Reduced N-doped graphene oxide aerogels preparation

GO was prepared by a modified Hummer method.[39] Briefly, 4 g of graphite, 2 g of $NaNO_3$ and 180 mL of H_2SO_4 were mixed and stirred vigorously for 3 h in a previously cooled round bottom flask placed in an ice bath for subsequent graphite pre-oxidation. Later, 11 g of $KMnO_4$ were added slowly and carefully, the ice bath was removed, and agitation was maintained for another two hours. To neutralize the oxidation process, first 180 mL of deionized water and then 30 mL of H_2O_2 were added drop by drop. Finally, the mixture was centrifugated and washed several times with deionized water to neutralize the GO mud and the solid was frozen and lyophilized to get GO dry flakes.

rGO monoliths were prepared by hydrothermal reduction of 10 mg/mL GO aqueous dispersions containing 10, 20, and 30 mg/mL of urea (samples rGO_N1, rGO_N2 and rGO_N3); these concentration ranges were like the used by Anjali et col.[40] In a typical experiment, 20 mL of an aqueous dispersion were frozen at −30 °C inside the vessel where the hydrothermal synthesis was going to be carried out. This process forces the system to gel before the hydrothermal process. Subsequently, the temperature of the hydrothermal reactor was increased up to 180 °C and kept for 7 h to form a hydrogel. Next, the reactor was cooled naturally, and the hydrogels were washed several times with distilled water to remove excess urea. The cryogels were formed from the hydrogels by freezing in a freezer at −30 °C and subsequently transformed into aerogels by freeze-drying. These aerogels were named GR_N0 (no urea), GR_N1, GR_N2, and GR_N3.

Aerogels were thermally treated at two temperatures (500 and 1000 °C) under N_2/H_2 atmosphere to study the influence of heat treatments on the doping processes and their electromagnetic properties. These two temperatures were selected as representative of the compositional and structural changes of aerogels induced by temperature (Figure S1).[41]

Techniques

SEM images were obtained with a Philips XL 30 scanning electron microscope. XRD analysis was accomplished by wide-angle X-Ray diffractometer (XRD, Panalytical X'pert Pro X-ray diffractometer) with Cu Kα radiation (λ = 0.15406 nm). XPS analysis of surfaces was performed using an XPS Spectrometer Kratos AXIS Supra. Survey and high-resolution spectra were obtained under UHV conditions. Raman spectroscopy was carried out with an NT-MDT NTegra Spectra micro-Raman confocal dispersive spectrometer, using the 532.348 nm laser excitation. For each sample, various spectra were recorded in different places to verify the homogeneity of the sample. Thermogravimetric analysis (TGA) was carried out using a simultaneous thermal analyser Perkin Elmer 6000 STA from room temperature to 1000 °C at 15 °C/min. The electrical properties of the aerogels were evaluated using an HP 34401 A source meter with 100 μΩ resolution in a 4-wire DC configuration to obviate the electrical resistance of the wires the temperature during the measurements was 25 °C.

Elemental analysis was carried out using a LECO CHNS-932.

The global electromagnetic shielding efficiency, SE_T, can be quantified as the sum of the contributions of reflection and

absorption mechanisms. For this purpose, the scattering parameters S_{11} and S_{21} were measured using a vector network analyser (Agilent, ENA, E5071) with a 7 mm coaxial transmission line adapter in the range of 1 to 18 GHz. An ENA instrument measures both the transmission coefficient as ($T = |S_{21}|^2 = |S_{12}|^2$) and the reflection coefficient as: ($R = |S_{11}|^2 = |S_{22}|^2$), therefore the absorption coefficient by the material (A) is:[42]

$$A = 1 - (R + T) \tag{1}$$

The ratios between the scattering parameters and the transmission, reflection, and absorption EMI shielding effectiveness are given by the following equations.[43]

$$SE_T = -10log(T) = -10log(|S_{21}|^2) \tag{2}$$

$$SE_R = -10log(1 - R) = -10log(1 - |S_{11}|^2) \tag{3}$$

$$SE_A = -10log\left(\frac{T}{1 - R}\right) = -10log\left(\frac{|S_{21}|^2}{1 - |S_{11}|^2}\right) \tag{4}$$

The scattering parameters were also used to calculate the complex magnetic permeability and dielectric permittivity. The measurements were performed according to the transmission/reflection method.[44] For electromagnetic characterization, the aerogels were vacuum infiltrated with a hydrogenated epoxy resin, as described previously,[1] cured and machined to the final required geometry for the coaxial line: rectangular toroid of nominal internal and external diameters close to 3.04 and 7 mm respectively. Sample thickness was fixed at 5 mm in all the cases to eliminate an extra variable that is widely known to affect the overall EMI shielding performance of the material, as can be observed in Figure S7 where some example samples are machined with two different thicknesses. Anyway, the influence of this sample feature is not the matter of this study and these plots are just shown as a representative example of what could happen if thickness is modified.[45]

Using the built-in software, a geometry correction was applied for small deviations from nominal geometry.[44]

Supporting Information

Supporting Information is available from the Wiley Online Library or from the author.

Acknowledgements

This work was supported by grant PID2021-125302NB-I00 from the Spanish Ministerio de Ciencia e Innovación.

Conflict of Interest

The authors declare no conflict of interest.

Data Availability Statement

The data that support the findings of this study are available from the corresponding author upon reasonable request.

Keywords: Conducting materials · Doping · gels · graphene · nanoparticles

[1] M. Crespo, N. Méndez, M. González, J. Baselga, J. Pozuelo, *Carbon* **2014**, *74*, 63–72.
[2] M. González, J. Pozuelo, J. Baselga, *Chem. Rec.* **2018**, *18*, 1000–1009.
[3] B. Zhao, M. Hamidinejad, S. Wang, P. Bai, R. Che, R. Zhang, C. B. Park, *J. Mater. Chem. A.* **2021**, *9*, 8896–8949.
[4] X. Xia, Y. Wang, Z. Zhong, G. J. Weng, *J. Appl. Phys.* **2016**, *120*, 085102.
[5] Z. Zhou, M. Li, H. Huang, L. Li, B. Yang, D. Yan, Z. Li, *ACS Appl. Mater. Interfaces* **2020**, *12*, 18840–18849.
[6] M. Crespo, M. González, A. L. Elías, *Phys. Status Solidi Rapid Res. Lett.* **2014**, *8*, 698–704.
[7] M. González, M. Crespo, J. Baselga, J. Pozuelo, *Nanoscale* **2016**, *8*, 10724–10730.
[8] S. Bi, L. Zhang, C. Mu, M. Liu, X. Hu, *Appl. Surf. Sci.* **2017**, *412*, 529–536.
[9] Z. Lin, J. Liu, W. Peng, Y. Zhu, Y. Zhao, K. Jiang, M. Peng, Y. Tan, *ACS Nano* **2020**, *14*, 2109–2117.
[10] F. Shahzad, M. Alhabeb, C. B. Hatter, B. Anasori, S. M. Hong, C. M. Koo, Y. Gogotsi, *Science* **2016**, *353*, 1137–1140.
[11] L. Liang, C. Yao, X. Yan, Y. Feng, X. Hao, B. Zhou, Y. Wang, J. Ma, C. Liu, C. Shen, *J. Mater. Chem. A* **2021**, *9*, 24560–24570.
[12] Y. Zhang, Y. Huang, H. Chen, Z. Huang, Y. Yang, P. Xiao, Y. Zhou, *Carbon* **2016**, *105*, 438–447.
[13] Y. Shang, H. Xu, M. Li, G. Zhang, *NANO* **2017**, *12*, 1750018.
[14] J. Zhou, Y. Chen, H. Li, R. Dugnani, Q. Du, H. UrRehman, H. Kang, H. Liu, *J. Mater. Sci.* **2017**, *53*, 4067.
[15] Y. Qin, J. Yuan, J. Li, D. Chen, Y. Kong, F. Chu, Y. Tao, M. Liu, *Adv. Mater.* **2015**, *27*, 5171–5175.
[16] I. K. Moon, S. Yoon, K. Chun, J. Oh, *Adv. Funct. Mater.* **2015**, *25*, 6976–6984.
[17] J. Li, X. Li, P. Zhao, D. Y. Lei, W. Li, J. Bai, Z. Ren, X. Xu, *Carbon* **2015**, *84*, 460–468.
[18] Y. Qing, Y. Li, F. Luo, *J. Mater. Sci. Mater. Electron.* **2020**, *32*, 25649–25655.
[19] R. Zan, A. Altuntepe, *J. Mol. Struct.* **2020**, *1199*, 127026.
[20] F. Sultanov, C. Daulbayev, B. Bakbolat, O. Daulbayev, *Adv. Colloid Interface Sci.* **2020**, *285*, 102281.
[21] X. Li, X. Yu, J. Liu, X. Fan, K. Zhang, H. Cai, N. Pan, X. Wang, *Chin. J. Chem. Phys.* **2012**, *25*, 325–329.
[22] M. Hu, Q. Lv, R. Lv, *ES. Energy. Environ.* **2019**, *3*, 45–54.
[23] J. Chen, Z. Mao, L. Zhang, Y. Tang, D. Wang, L. Bie, B. D. Fahlman, *Carbon* **2018**, *130*, 41–47.
[24] G. Waller, Y. Liu, M. Liu, C. Wong, *Adv. Energy Mater.* **2012**, *2*, 884–888.
[25] Z. Jia, M. Zhang, B. Liu, F. Wang, G. Wei, Z. Su, *ACS Appl. Nano Mater.* **2020**, *3*, 6140.
[26] T. Lin, W. Lai, Q. Lü, Y. Yu, *Electrochim. Acta* **2015**, *178*, 517–524.
[27] F. F. Hassan, V. Chabot, J. Li, B. K. Kim, L. Ricardez-Sandoval, A. Yu, *J. Mater. Chem. A* **2013**, *1*, 2904.
[28] P. Liu, Y. Zhang, J. Yan, Y. Huang, L. Xia, Z. Guang, *Chem. Eng. J.* **2019**, *368*, 285–298.
[29] National Institutes of Health, ImageJ image processing and analysis in java, **2019**.
[30] X. Feng, *Nanocarbons for advanced energy conversion*, vol. 2, Wiley-VCH, Hoboken, NJ, USA, **2015**.
[31] N. P. D. Ngidi, M. A. Ollengo, V. O. Nyamori, *Materials* **2019**, *12*, 3376.
[32] H. Wang, T. Maiyalagan, X. Wang, *ACS Catal.* **2012**, *2*, 781–796.
[33] T. H. Nguyen, D. Yang, B. Zhu, H. Lin, T. Ma, B. Jia, *J. Mater. Chem. A* **2021**, *9*, 7366–7395.
[34] F. H. B. Baldovino, A. T. Quitain, N. P. Dugos, S. A. Roces, M. Koinuma, M. Yuasa, T. Kida, *RSC Adv.* **2017**, *7*, 3852.
[35] F. Chen, L. Guo, X. Zhang, Z. Y. Leong, S. Yang, H. Y. Yang, *Nanoscale* **2017**, *9*, 326–333.
[36] Z. Mou, X. Chen, Y. Du, X. Wang, S. Wang, P. Yang, *Appl. Surf. Sci.* **2011**, *258*, 1704–1710.

[37] P. Xu, X. Han, C. Wang, D. Zhou, Z. Lv, A. Wen, X. Wang, B. Zhang, *J. Mater. Chem. B* **2008**, *112*, 10443–10448.
[38] A. C. R. Fernández, N. J. Castellani, *Surf. Sci.* **2020**, *693*, 121546.
[39] L. Sun, L. Wang, C. Tian, T. Tan, Y. Xie, K. Shie, K. Shi, M. Li, H. Fu, *RSC Adv.* **2012**, *2*, 4498.
[40] J. Anjali, V. K. Jose, J. Lee, *J. Mater. Chem. A* **2019**, *7*, 15491–15518.
[41] M. Gonzalez, J. Baselga, J. Pozuelo, *Carbon* **2019**, *147*, 27–34.
[42] M. Cao, W. Song, Z. Hou, B. Wen, J. Yuan, *Carbon* **2010**, *48*, 788–796.
[43] M. Cao, C. Han, X. Wang, M. Zhang, Y. Zhang, J. Shu, H. X. Fang, J. Yuan, *J. Mater. Chem. C* **2018**, *6*, 4586–462.
[44] Agilent Technologies, Agil 85071E, Mater. Meas. Software, **2013**.
[45] D.-s. Li, S.-j. Wang, Y. Zhou, L. Jiang, *Nanotechnol. Rev.* **2022**, *11*, 1722–1732. https://doi.org/10.1515/ntrev-2022-0088.

Manuscript received: September 29, 2022
Revised manuscript received: November 2, 2022
Accepted manuscript online: November 4, 2022
Version of record online: December 8, 2022